ACS NANO

www.acsnano.org

ARTICLE

Emerging Nontrivial Topology in Ultrathin Films of Rare-Earth Pnictides

Dai Q. Ho,* Ruiqi Hu, D. Quang To, Garnett W. Bryant,* and Anderson Janotti*

Cite This: *ACS Nano* 2023, 17, 20991−20998

Read Online

ACCESS | Metrics & More | Article Recommendations | Supporting Information

ABSTRACT: **Thin films of rare-earth monopnictide (RE-V) semimetals are expected to turn into semiconductors due to quantum confinement effects (QCE), lifting the overlap between electron pockets at Brillouin zone edges (X) and hole pockets at the zone center (Γ). Instead, using LaSb as an example, we find the emergence of the quantum spin Hall (QSH) insulator phase in (001)-oriented films as the thickness is reduced to 7, 5, or 3 monolayers (MLs). This is attributed to a strong QCE on the in-plane electron pockets and the lack of quantum confinement on the out-of-plane pocket projected onto the zone center, resulting in a band inversion. Spin−orbit coupling (SOC) opens a sizable nontrivial gap in the band structure of ultrathin films. Such effect is anticipated to be general in rare-earth monopnictides and may lead to interesting phenomena when coupled with the 4*f* magnetic moments present in other members of this family of materials.**

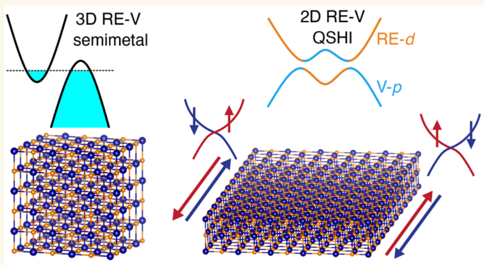

KEYWORDS: *rare-earth monopnictide, quantum spin Hall insulator, even and odd band gap oscillation, quantum confinement effect, thin film*

Rare-earth monopnictides, with a simple rock-salt crystal structure shown in Figure 1a, are fully compensated semimetals with electron pockets centered at three X points and two hole pockets at Γ, as shown in Figure 1b for LaSb. RE-V thin films have been epitaxially grown on III−V semiconductors (III−Vs).[1−3] These films are sought as structurally perfect, lattice-matched epitaxial contacts to III−Vs,[1,4,5] as well as nanoparticles embedded in III−Vs for thermoelectric and terahertz applications.[5−10] Some members of this family of materials display other interesting properties such as extremely large magnetoresistance and nontrivial topological phase, including the recently observed Fermi arcs due to magnetic splitting in the antiferromagnet NdBi.[11−18] The relatively small overlap in energy between the electron and hole pockets results in modest carrier densities and has led researchers to anticipate that this overlap could be lifted and a band gap opened in structures with reduced dimensions, such as nanoparticles or thin films, as a result of quantum confinement effects.[7,8,19] However, to date, these expectations have not been met, and the reasons for this remain unknown.

Through first-principles calculations for thin films of LaSb(001) (used as a representative of this class of materials), we show that an orbital-selective quantum confinement effect ultimately leads to a quantum spin Hall phase for films that are 7, 5, or 3 monolayers thick, with an inverted band gap in the bulk and helical spin-momentum locked edge states. Calculations of the $\mathbb{Z}_2$ topological invariant, spin-resolved band structure of a nanoribbon and a semi-infinite ribbon confirm the nontrivial topology in these ultrathin films. Our calculations reveal how quantum confinement selectively affects the electron pockets lying along the plane of the film (denoted by α and centered at X_x and X_y, see Figure 1b−d) and along the normal direction (centered at X_z), and explain the semimetallic behavior of thin films that ultimately transform into a QSH phase as the thickness is reduced to 7-ML or less. These results contribute to advancing the realization of intrinsic QSH phases in wafer-scale material systems, adding to the demonstrations based on HgCdTe/CdTe quantum wells[20,21] and monolayer transition-metal dichalcogenides,[22−26] as well as some other recent proposals.[27−29]

RESULTS AND DISCUSSION

The band structure of bulk LaSb using the 2-atom primitive cell is shown in Figure 1d. More detailed orbital-resolved band structures are shown in Figure S1−S3. There are three electron pockets, centering at X_x, X_y, and X_z, that are bands derived from La 5*d* orbitals and two hole pockets (β and δ, centered at

Received: April 12, 2023
Revised: October 13, 2023
Accepted: October 16, 2023
Published: October 23, 2023

https://doi.org/10.1021/acsnano.3c03307
ACS Nano 2023, 17, 20991−20998

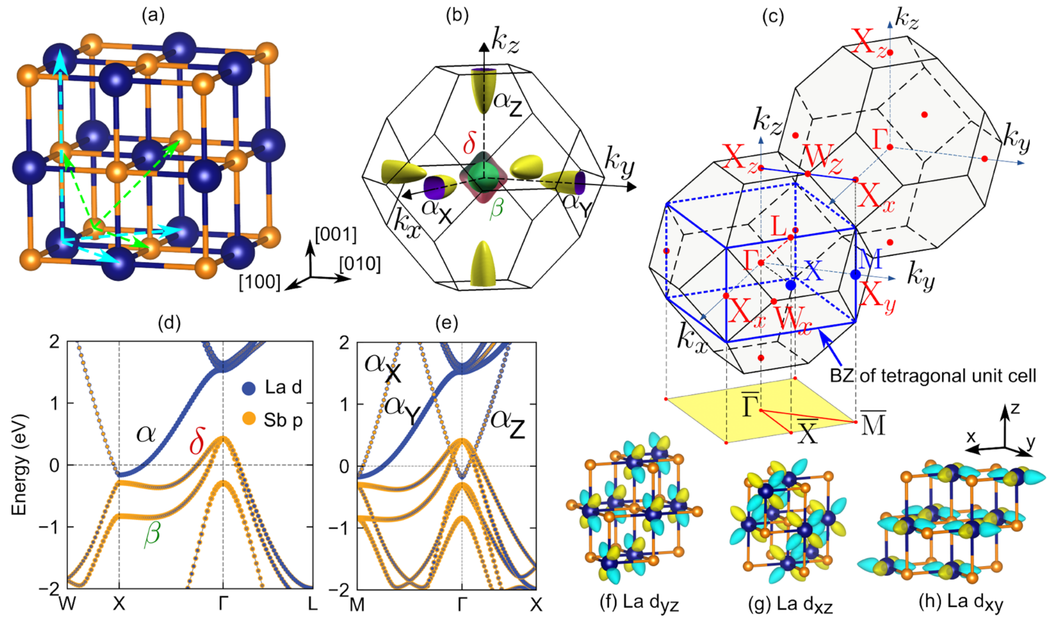

Figure 1. Structure and electronic properties of LaSb, representative of a typical semimetallic RE-V. (a) Conventional rock-salt crystal structure, the green and cyan arrows representing the unit vectors of the bulk primitive unit cell and tetragonal unit cell, respectively. (b) Fermi surface of semimetallic RE-V featuring two hole pockets at Γ and three equivalent electron pockets at X points. (c) 3D Brillouin zone (BZ) of RE-V *fcc* crystal structure and its projection onto (001) plane (yellow plane); also shown is the 3D BZ of the tetragonal unit cell (blue square prism inside the BZ of the primitive *fcc* cell). (d) Band structure of bulk LaSb using a primitive unit cell exhibiting major contribution from La *d* bands to electron pockets and Sb *p* bands to hole pockets, and (e) using a 4-atom tetragonal unit cell showing the band folding (M and X points in blue in c). Visualization of the wave functions of the electron pockets centered at (f) X_x, (g) X_y, and (h) X_z (yellow and cyan lobes represent the + and − signs of the wave functions).

Γ) derived from Sb 5*p* orbitals crossing the Fermi level, and leading to full compensation, i.e., the total numbers of electrons and holes are equal. This overlap is overestimated in Generalized Gradient Approximation functionals of Density Functional Theory (DFT-GGA), resulting in artificially higher carrier concentrations compared to experimental values, while the screened range-separated hybrid functional of Heyd−Scuseria−Ernzerhof (HSE06) gives carrier concentrations in better agreement with experiments.[30] As can be seen in Figure 1b, the electron pockets are highly anisotropic with each ellipsoid's semimajor axis along the corresponding Cartesian axis, and the semiminor axis perpendicular to it. The hole pockets, however, are more isotropic with the inner spherical-like pocket β and the outer warped double pyramid pocket δ. In the following, we show that the quantum confinement in thin films selectively affects the electron and hole pockets, according to their effective masses (band curvature) and the directional distribution of the corresponding wave functions, leading to band inversions and the emergence of the QSH phase in ultrathin films.

The electronic band structure of a free-standing slab with 15 monolayers (15-ML) is shown in Figure 2a, along $\overline{M}-\overline{\Gamma}-\overline{X}$, where $\overline{M}$ is the projection of the two high symmetry points X_y and X_x, $\overline{\Gamma}$ is the projection of Γ and X_z, and $\overline{X}$ is the projection of the L points onto the 2D BZ of the thin films (Figure 1c). We note that the electron pockets at $\overline{M}$ (corresponding to X_x and X_y) are shifted upward in energy while the electron pocket at $\overline{\Gamma}$ (projected from X_z) remains nearly unchanged. At the $\overline{M}$ point, there are two sets of electron pocket subbands with quite different dispersions: one set has low dispersion (high effective mass), while the other set exhibits large dispersion (low effective mass).

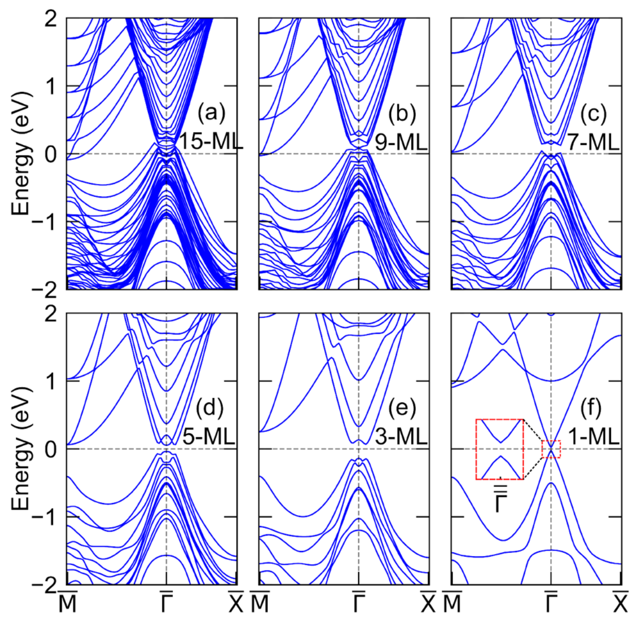

Figure 2. Electronic structure of freestanding films of LaSb with the thickness of (a) 15-ML, (b) 9-ML, (c) 7-ML, (d) 5-ML, (e) 3-ML, (f) 1-ML. Due to the orbital-selective quantum confinement effect on the electron pockets at $\overline{M}$ and $\overline{\Gamma}$, a phase transition from topologically trivial semimetal in 15-ML film to nontrivial insulator in 7-, 5-, 3-ML films and eventually trivial insulator in 1-ML film can be observed. The inset in f shows a noninverted gap of 44 meV in 1-ML film.

The electronic structure of the 9-ML thick slab is shown in Figure 2b, indicating a semimetal on the brink of having an electron pocket at $\overline{M}$ above the Fermi level. For the 7-ML and 5-ML thick slabs, Figure 2c,d show that the electron pockets at $\overline{M}$ are above the Fermi level due to the QCE, and inverted band gaps at $\overline{\Gamma}$ are opened in the presence of SOC, indicating the emergence of a 2D (or quasi 2D) QSH insulator phase.[20,31,32] The gaps at $\overline{M}$ and $\overline{\Gamma}$ are larger in the 3-ML thick film (Figure 2e). At the ultimate limit of 1-ML thick, the LaSb film becomes a normal insulator thanks to the quantum confinement lifting up the overlap (at $\overline{\Gamma}$) between the projected electron pocket from X_z and hole pockets, leading to a normal band ordering (Figure 2f, the inset shows a trivial gap of 44 meV).

As described above, the electronic structure of LaSb films evolves from a semimetal with trivial topology to a nontrivial insulator as the film thickness decreases to a few MLs. The topologically nontrivial electronic structure follows a band inversion, as shown in Figure 3b for the case of 3-ML thick film. To confirm the nontrivial topological nature of the 3-ML LaSb film, we calculated the $\mathbb{Z}_2$ topological invariant using the Fu−Kane formula (parity criteria)[33] as well as the Fukui−Hatsugai method,[34] obtaining $\mathbb{Z}_2 = 1$. The topological characteristic is further corroborated by following the evolution of the Wannier charge center (WCC) as a function of momentum, shown in Figure 3c, indicating the topological nontriviality as the red-dashed reference line cuts through the WCC evolution line an odd number of times.

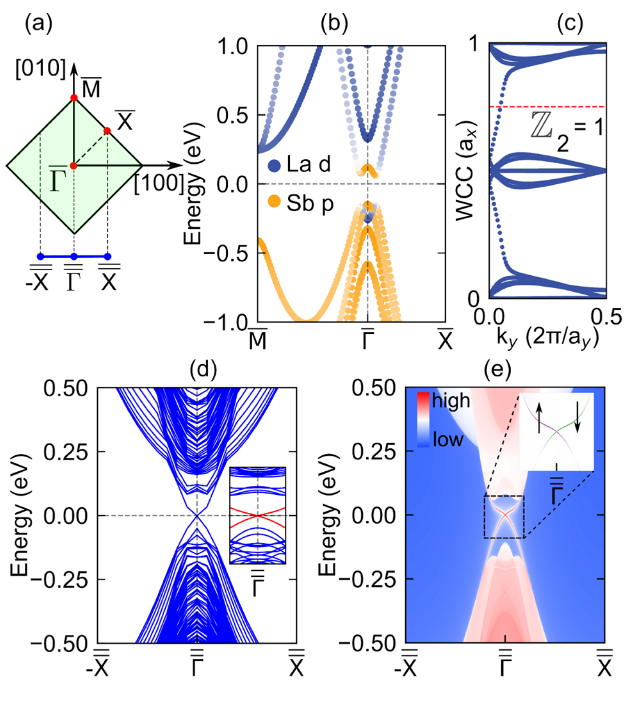

Figure 3. Signature of the quantum spin Hall insulating phase in the LaSb 3-ML thick film. (a) 2D BZ of the thin film and 1D BZ of the corresponding ribbon (blue line) with the periodic direction along *x*. (b) Projected band structure near the Fermi level (set at 0 eV) displaying an inverted band gap at $\overline{\Gamma}$, and (c) the Wannier charge center evolution of the 3-ML thick freestanding film exhibiting the nontrivial topological property as the red dashed reference line crossing the evolution line (represented by filled blue circles) an odd number of times. (d) Electronic structure of the ribbon made from the 3-ML thick film showing the presence of edge states crossing at Fermi level as highlighted by red lines in the inset, and (e) electronic structure of a semi-infinite wide ribbon made from the 3-ML thick LaSb film obtained from Wannier orbital-based Tight-binding Hamiltonian and the spin-resolved edge states shown in the inset.

Based on the bulk-boundary correspondence, we expect the existence of spin-momentum locked edge states in the QSH insulator phase of LaSb(001) ultrathin films.[31] We searched for the presence of these spin-polarized edge states by calculating the band structure of a nanoribbon cut from the 3-ML infinite film along the [100] direction. We found that the nanoribbon must be at least 50 MLs wide (∼16 nm) to avoid interactions between the two opposite edges of the ribbon. The electronic structure of the 3-ML thick, 50-ML wide nanoribbon is shown in Figure 3d, where the edge states cross at the 4-fold degenerate Dirac point $\overline{\overline{\Gamma}}$, represented by a pair of red lines in the vicinity of $\overline{\overline{\Gamma}}$ in the inset. The corresponding spin-resolved electronic structure in Figure 3e, obtained by the iterative surface Green's function method,[35] for a semi-infinite ribbon structure, and the spatial distribution of spin-resolved wave functions of edge states shown in Figure S4, clearly demonstrate the helical spin-momentum locking of the edge modes, thus confirming the presence of the QSH insulator phase in the 3-ML thick film.

For 7-ML or 5-ML thick films, there are two sets of band inversions (see Figure S5a,e), thus no time-reversal symmetry-protected edge states are expected, i.e., spin scattering from spin-up to spin-down channels on the same edge is possible.[36,37] Therefore, they are classified as trivial band insulators with the topological invariant $\mathbb{Z}_2 = 0$. However, one pair of inverted bands can be removed when a small biaxial tensile strain is applied to films deposited on an appropriately chosen substrate. Such an approach has been investigated theoretically[38] and recently demonstrated experimentally in the case of RE-Vs grown on III−V substrates.[39] This biaxial (or epitaxial) strain allows for selective lifting of the overlap between one pair of electron and hole subbands, resulting in an odd number of band inversions so that a QSH insulator phase can also be realized in 5-ML and 7-ML thick films (see Figure S5c,d,g,h).

To understand the electronic structure of (001)-oriented films, we turn to the band structure of LaSb in the tetragonal unit cell, with two formula units, at $k_z = 0$, as shown in Figure 1e, since it has the same symmetry as that of the (001)-oriented films, i.e., we can build an (001)-oriented film unit cell from the tetragonal unit cell. Its corresponding BZ is highlighted by the blue square prism inside the BZ of the primitive cell in Figure 1c. The electron pocket at Γ, overlapping in momentum and energy with the hole pockets, corresponds to the pocket at X_z due to the folding of the BZ along k_z (see more details in the orbital-resolved band structures in Figure S1−S3, especially Figure S1b, S2c, S3c). It can also be viewed as the projection on the k_x−k_y plane of the ellipsoid along k_z in the Fermi surface of the primitive cell (Figure 1b).

At the M point in Figure 1e, there are two electron bands with different dispersions: the lower dispersion band composed of La d_{xz} (Figure S1b and S2a), originally from the pocket at X_y, with the dispersion along the semimajor axis Γ−X_y, and the higher dispersion counterpart originating from the projection of the semiminor axis X_x−W_z of the pocket at X_x from the adjacent BZ (the path connecting X_x to X_z and highlighted in blue in Figure 1c). Thus, the three electron pockets in the BZ of the primitive cell reside in two locations in the BZ of the tetragonal unit cell, i.e., X_x and X_y at M, and X_z at Γ, and

https://doi.org/10.1021/acsnano.3c03307
ACS Nano 2023, 17, 20991−20998

ultimately dictate the effects of quantum confinement upon reduction of the film thickness.

The two electron pockets at M in the bulk give rise to subbands in the (001)-oriented thin films at $\overline{M}$. The low-dispersion set of subbands originates from the La d_{xz} orbital interaction taking place along the semimajor axis $\Gamma-X_y$, while the high dispersion set of subbands originates from the semiminor axis X_x-W_z due to the in-plane interaction of La d_{yz}, featuring a stronger interaction and hence a smaller effective mass. Thus, the gaps at the X_x and X_y points in the bulk correspond to the gap at the $\overline{M}$ point in the thin film, and the energy separation of the subbands at $\overline{M}$ is associated with the dispersion, or effective mass, of the electron band at X_x (X_y). At $\overline{\Gamma}$, however, the electron pocket, projected from X_z, overlaps with hole pockets. Since these electron bands are composed of La d_{xy} orbitals, the wave functions are distributed in the plane of the film and, therefore, are not affected by the reduction in the film thickness, maintaining its semimetallic character until the thickness reaches 7 or fewer ML, at which point a gap emerges due to the band inversion and SOC.

The transition from the trivial semimetal to the QSH phase as the thickness is reduced in the thin films can be understood by analyzing the effects of quantum confinement on the electron pockets at X_x, X_y, and X_z. The spatial distribution of the single-particle wave functions at the three X points is shown in Figure 1f–h. At X_x (X_y), the wave function is composed of La d_{yz} (d_{xz}) orbitals (Figure S1b), resulting in a low dispersion along the semimajor axis $\Gamma-X_x$ ($\Gamma-X_y$) since most of the orbital interaction occurs along the direction normal to their charge distribution, as depicted in Figure 1f,g. Meanwhile, the same band has a higher dispersion along the perpendicular direction, i.e., the electron pocket's semiminor axis X−W, thanks to the strong orbital interaction in the plane of their distribution (*yz* and *xz* planes for pockets at X_x and X_y, respectively). At X_z, on the other hand, the wave function is composed of La d_{xy} orbital, i.e., lying in the *xy* plane and with small overlap along the [001] or *z* direction (Figure 1h). Therefore, the quantum confinement in (001)-oriented thin films will affect mostly the electron pockets whose wave functions are largely distributed in the planes perpendicular to the film, i.e., the pockets centered at X_x and X_y; the electron pocket at X_z will be marginally affected as the thickness of the film is reduced because the corresponding wave function is spread mostly in the plane of the film.[40,41]

Taking a closer look at the thickness-dependence of the electronic structure of the thin films, there is a striking difference between films having even and odd numbers of monolayers (Figure 4 and S6), particularly near the Fermi level. As the thickness of the film decreases, the QCE is stronger, resulting in gradually larger subband separations. The quantum confinement also affects the size of the gap at the $\overline{M}$ and $\overline{\Gamma}$ points, which oscillates when going from an odd to an even number of ML, as shown in Figure S6 and Figure 4, respectively.

The variation in the gap size of the thin films around the $\overline{\Gamma}$ point with odd and even numbers of MLs can be explained by the difference in their symmetry. The films having an odd number of MLs belong to a symmorphic symmetry group (space group number 123 with point group *P*4/*mmm*) while the films with an even number of MLs possess a non-symmorphic symmetry group (space group number 129 with point group *P*4/*nmm*). This leads to a distinction in the symmetry of the bands around the Fermi level, as shown in

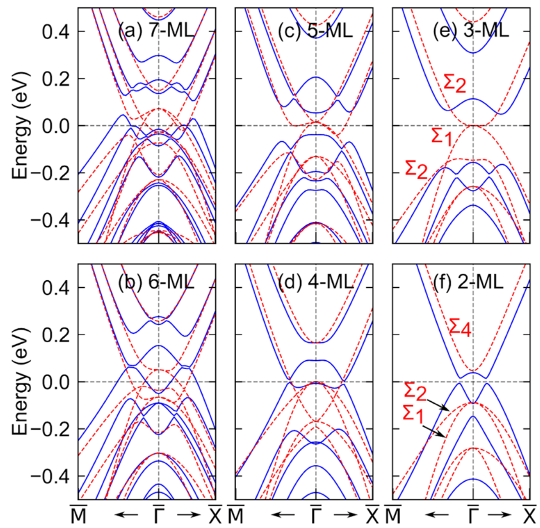

Figure 4. Electronic structures in the proximity of the $\overline{\Gamma}$ point of LaSb freestanding thin films with an even/odd number of MLs. Red dashed lines and blue lines indicate bands without and with SOC, respectively. Irreps of relevant bands are denoted by capitalized Greek letters.

Figure 4e,f taking 3-ML and 2-ML films as examples. For the 3-ML film, one electron band and two hole bands overlap in the proximity of $\overline{\Gamma}$, leading to a band inversion at $\overline{\Gamma}$ in the absence of SOC (represented by red dashed lines). Crucially, one of the hole bands has the same symmetry as that of the electron band (irrep Σ_2, Figure 4e), leading to a gap opening due to their mutual interaction. However, the other hole band with a different irrep (Σ_1) does not interact with the electron counterpart, resulting in a semimetallic phase with a degeneracy of the two hole bands at the $\overline{\Gamma}$ point (see more detail in Figure S7). This inverted band gap semimetal with a degenerate point at the zone center is similar to bulk HgTe,[20] giving rise to a topological semimetal phase. The degeneracy in bulk HgTe is protected by its crystal symmetry and is stable even in the presence of SOC; it is only lifted, and a tiny gap opens when the bulk crystal symmetry is broken, i.e., in the thin film structure (quantum well). For the 3-ML LaSb film, however, the degeneracy is not stable under the influence of SOC since it can be considered as a projection from the original degeneracy of the top two hole bands at the X_z point of the bulk when SOC is not taking into consideration. As a consequence, when turning on SOC, a sizable inverted gap comparable to the SOC splitting between β and δ bands at the bulk X point is observed, resulting in a nontrivial topological phase as described above.

On the other hand, for the 2-ML film, the two hole bands and the electron band have different symmetries, characterized by irreps Σ_1, Σ_2, and Σ_4, respectively (Figure 4f). Therefore, in the absence of SOC, those bands would cross if they were overlapping in energy since their interactions are prohibited by symmetry, i.e., as in the case of the 4-ML thick film shown in Figure 4d without SOC. When SOC is turned on, the highest hole band and the electron band overlap in energy, leading to an SOC-induced gap opening. However, this gap is tiny since the SOC represents only a small perturbation, the relevant orbital interaction is not allowed by symmetry. Similar arguments can be applied to understand the sizable inverted gaps in the other films with odd number of MLs such as the 5-

https://doi.org/10.1021/acsnano.3c03307
ACS Nano 2023, 17, 20991−20998

ML and 7-ML, as well as the calculated essentially zero gaps in the films with even number of MLs such as the 4-ML and 6-ML films.

The effects discussed here are expected to occur for all materials in the family of RE-Vs with RE = Sc, Y, La, ..., Lu and V = As, Sb, Bi since they have the same crystal structure and similar orbital composition of the bands near the Fermi level. Note, however, that some of the Bi-based compounds already show nontrivial topology in the 3D bulk due to the crossing of the Bi 6*p* and the rare-earth 5*d* bands near the X point.[15,16] The As- and Sb-based compounds are all topologically trivial semimetals and hence are all expected to become topologically nontrivial when made as few monolayers thick, (001)-oriented ultrathin films. Apart from the case of Sc-, Y-, La-, and Lu-based compounds, where the RE 4*f* orbitals are completely empty or filled, other RE-Vs exhibit magnetic ordering at low temperatures.[42−45] This creates an opportunity to combine nontrivial topology with spin magnetism, potentially leading to the emergence of novel phenomena such as 2D antiferromagnetic topological insulators,[46−48] the quantum anomalous Hall effect in Chern insulators,[49,50] and the presence of Fermi arcs resulting from an unconventional magnetic splitting.[18] Further discussion on the effect of partially filled 4*f* states is provided in Supporting Information, Note S2.

Experiments have already demonstrated the epitaxial growth of RE-Vs thin films on conventional III−V substrates down to a few MLs thick. Scanning tunneling spectroscopy measurements on GdSb/GaSb has explored the possibility of turning GdSb semimetal into a semiconductor in ultrathin films, yet failing.[39,51] The authors, however, were not searching for edge states at that time. We also note that the presence of metallic interface states at the interface RE-Vs/III−Vs[52] might lead to difficulties in identifying the spin-momentum locked edge states and that perhaps a different substrate with different bonding at the interface might be required. In the case of LaSb, the utilization of rock-salt substrates such as MgTe, CaTe, or SrTe is recommended, as these materials would help mitigate the presence of interface metallic states, thereby facilitating the observation of the spin-momentum locked edge states in the RE-Vs thin films.

CONCLUSIONS

In conclusion, we investigated the electronic structure of nonmagnetic RE-Vs thin films at various thicknesses using first-principles calculations employing the hybrid functional HSE06, taking LaSb as a case study. At the limit of 3-ML, we find the emergence of the QSH insulator phase characterized by the nontrivial $\mathbb{Z}_2$ topological invariant and the presence of helical spin-momentum locked edge states. Similar results can be obtained for 5-ML and 7-ML films with an applied small biaxial tensile strain. The quantum confinement in (001)-oriented thin films has dissimilar effects on the electron pockets centered at equivalent X points at the zone edges, owing to their orbital composition. The directional nature of the wave function associated with the electron pocket at X_z point, distributed mainly in the plane of the film, with weak out-of-plane interactions, makes this pocket resistant to finite size effects, leading to a band inversion, and a gap that opens due to SOC, in the limit of very thin films. Our results indicate that this effect is general for the RE-Vs, with a possibly interesting combination of 4*f* magnetism with nontrivial topological band structures in ultrathin films.

COMPUTATIONAL METHODS

First-principles calculations based on density functional theory[53,54] as implemented in the VASP code[55,56] have been performed for structural optimization and electronic structure calculations. The projector augmented-wave (PAW) method was used to describe the ion core and valence electrons interaction.[57,58] The screened hybrid exchange-correlation functional of Heyd−Scuseria−Ernzerhof (HSE06)[59,60] was employed in all cases except the calculations of the electronic structures of nanoribbons because these calculations required very large unit cells. In that case, the generalized gradient approximation (GGA) functional of Perdew−Burke−Ernzerhof (PBE)[61,62] was used instead. A plane-wave basis set with up to kinetic cutoff energy of 400 eV, and 12 × 12 × 12 *k*-point mesh for bulk LaSb and 10 × 10 × 1 *k*-point mesh for thin films were used, respectively. Due to large unit cell sizes of the LaSb nanoribbons, first-principles calculations searching for the presence of edge states were performed using the OpenMX code.[63−65] The code employs a linear combination of pseudoatomic orbitals (LCPAO) as a basis set to describe the electronic wave functions and reliable fully relativistic norm-conserving pseudopotentials to accurately model the electron−ion interaction.[66] In addition, OpenMX achieves computational efficiency by utilizing efficient algorithms such as fast Fourier transforms and density matrix techniques to solve the Kohn−Sham equations. We have used La8.0-s3p2d2f1 and Sb7.0-s3p2d2 basis sets to expand the electronic wave functions, and sampled the BZ of nanoribbons with a regular *k*-point mesh of 8 × 1 × 1. Cutoff energy value up to 220 Ry was used in numerical integrations and the solution of Poisson's equation. Spin−orbit coupling was self-consistently considered in all calculations, unless otherwise stated.

To efficiently evaluate the bulk-edge correspondence, maximally localized Wannier functions (MLWFs) based effective Hamiltonians were constructed by wannierizing the HSE06 first-principles calculations, taking La *d* and Sb *p* as projectors, using Wannier90 code.[67] A high-quality effective Hamiltonian was obtained by an almost perfect matching of electronic band structures from an MLWF-based Hamiltonian and first-principles calculations as well as the observation that the obtained Wannier functions are well localized. Edge state spectra were then calculated by using the surface Green's function in iterative approach for semi-infinite systems[35] as implemented in WannierTools.[68] Using MLWFs in iterative calculations of the surface Green's function offers several advantages such as providing a compact basis set that reduces computational complexity while allowing for an accurate representation of surface electronic states. Their exponential localization aids convergence in the iterative technique, leading to faster and more accurate calculations. Given a set of Wannier functions, their charge centers are defined as the average positions of charge of the Wannier functions that reside in the home unit cell. The winding of Wannier charge centers in momentum space and the winding of Wannier functions in real space are geometrically linked. When the Wannier charge centers wind around a momentum direction in the Brillouin zone, this implies that the corresponding Wannier functions are undergoing a spatial winding or rotation in real space. The spatial winding of Wannier functions can indicate the presence of nontrivial topological properties in the material, such as the emergence of edge states or the presence of a nonzero Chern number.[69,70] Within the context of a 2D topological insulator, the displacement of WCC can be used to describe the topological property of an electronic band structure since it is relevant to the change in the Berry phase, i.e., both quantities can be expressed in terms of Berry connection.[69,71] Furthermore, in systems preserving both time reversal symmetry and space inversion center, the topological invariant $\mathbb{Z}_2$ number can be obtained using the Fu−Kane formula (the parity criteria) by taking the product of parity eigenvalues of all occupied bands (take one for each Kramers pair) at time reversal symmetry momenta.[33] The eigenvalue of the parity operator and symmetry irreducible representations (irreps) of electronic bands were determined using the irvsp code.[72] The method developed by Fukui and Hatsugai for computing $\mathbb{Z}_2$ invariants, which integrates the formula established by

https://doi.org/10.1021/acsnano.3c03307
ACS Nano 2023, 17, 20991−20998

Fu and Kane and incorporates advancements in computing Chern numbers within a lattice Brillouin zone through the utilization of lattice gauge theory, was also employed to confirm the material's topological property.[34]

The calculated lattice parameter of bulk LaSb is 6.547 Å using DFT-GGA and 6.518 Å using the HSE06 hybrid functional, in good agreement with previous calculations[30] and the experimental value of 6.488 Å;[73] the latter was adopted in the present study. Thin films were simulated by using the supercell approach. The film structures were built based on the tetragonal unit cell of bulk LaSb and adjusting the number of single layers (or monolayers). A vacuum spacing larger than 20 Å was added along the [001] direction to avoid spurious interactions between periodically repeated image cells along that direction. In the case of 5-ML and 7-ML films, we also applied (001) biaxial tensile strain of (1% to 3%, and 3% to 5%, respectively) to tune the band gap and the topology. Nanoribbon structures were built by selecting a single periodic dimension, i.e., the [100] direction, and a finite width in the perpendicular direction within the film plane, i.e., the [010] direction. All of the atoms in the supercells were allowed to relax until the forces on each atom converge to a threshold smaller than 0.01 eV/Å while keeping the lattice constants of the supercell fixed.

ASSOCIATED CONTENT

Supporting Information

The Supporting Information is available free of charge at https://pubs.acs.org/doi/10.1021/acsnano.3c03307.

> Additional details on the discussion of the suitability and applicability of the theoretical method (Note S1), generalization to other RE-V compounds (Note S2); orbital-resolved (projected) band structures of bulk LaSb primitive unit cell, 4-atoms tetragonal unit cell, free-standing film with a thickness of 15-MLs; spatial distribution of spin-resolved wave functions of edge states in 3-ML thick, 50-ML wide LaSb nanoribbon; the evolution of the topology of electronic structures in LaSb thin films with 5-ML and 7-ML thick under biaxial tensile strain; electronic band structures in the whole Brillouin zone of even and odd number of MLs system; SOC-induced nontrivial gap opening mechanism in LaSb 3-ML system; and additional calculations for other members of RE-V compounds such as ErAs and LuBi (PDF)

AUTHOR INFORMATION

Corresponding Authors

Dai Q. Ho − *Department of Materials Science and Engineering, University of Delaware, Newark, Delaware 19716, United States; Faculty of Natural Sciences, Quy Nhon University, Quy Nhon 590000, Vietnam;* orcid.org/0000-0002-3282-5862; Email: daiqho@udel.edu

Garnett W. Bryant − *Nanoscale Device Characterization Division, Joint Quantum Institute, National Institute of Standards and Technology, Gaithersburg, Maryland 20899-8423, United States; University of Maryland, College Park, Maryland 20742, United States;* Email: garnett.bryant@nist.gov

Anderson Janotti − *Department of Materials Science and Engineering, University of Delaware, Newark, Delaware 19716, United States;* orcid.org/0000-0002-0358-2101; Email: janotti@udel.edu

Authors

Ruiqi Hu − *Department of Materials Science and Engineering, University of Delaware, Newark, Delaware 19716, United States;* orcid.org/0000-0003-0596-1217

D. Quang To − *Department of Materials Science and Engineering, University of Delaware, Newark, Delaware 19716, United States*

Complete contact information is available at: https://pubs.acs.org/10.1021/acsnano.3c03307

Notes

The authors declare no competing financial interest.

ACKNOWLEDGMENTS

We thank C. J. Palmstrøm, S. Khalid, and H. S. Inbar for fruitful discussions. This work was supported by the NSF through the UD-CHARM University of Delaware Materials Research Science and Engineering Center (MRSEC) Grant No. DMR-2011824. A.J. acknowledges support from the U.S. Department of Energy (Contract No. DE-SC0014388). We also acknowledge the use of Bridges-2 at PSC through allocation DMR150099 from the Advanced Cyberinfrastructure Coordination Ecosystem: Services & Support (ACCESS) program, which is supported by National Science Foundation Grants No. 2138259, 2138286, 2138307, 2137603, and 2138296, and the DARWIN computing system at the University of Delaware, which is supported by the NSF Grant No. 1919839.

REFERENCES

(1) Palmstrøm, C.; Tabatabaie, N.; Allen, S., Jr. Epitaxial Growth of ErAs on (100) GaAs. *Appl. Phys. Lett.* **1988**, *53*, 2608−2610.

(2) Buehl, T. E.; LeBeau, J. M.; Stemmer, S.; Scarpulla, M. A.; Palmstrøm, C. J.; Gossard, A. C. Growth of Embedded ErAs Nanorods on (411)A and (411)B GaAs by Molecular Beam Epitaxy. *J. Cryst. Growth* **2010**, *312*, 2089−2092.

(3) Kawasaki, J. K.; Schultz, B. D.; Lu, H.; Gossard, A. C.; Palmstrøm, C. J. Surface-Mediated Tunable Self-Assembly of Single-Crystal Semimetallic ErSb/GaSb Nanocomposite Structures. *Nano Lett.* **2013**, *13*, 2895−2901.

(4) Hanson, M.; Gossard, A.; Brown, E. ErAs As a Transparent Contact at 1.55 μm. *Appl. Phys. Lett.* **2006**, *89*, 111908.

(5) Bomberger, C. C.; Lewis, M. R.; Vanderhoef, L. R.; Doty, M. F.; Zide, J. M. Overview of Lanthanide Pnictide Films and Nanoparticles Epitaxially Incorporated into III−V Semiconductors. *J. Vac. Sci. Technol., B: Nanotechnol. Microelectron.: Mater., Process., Meas., Phenom.* **2017**, *35*, 030801.

(6) Liu, X.; Ramu, A.; Bowers, J. E.; Palmstrøm, C.; Burke, P. G.; Lu, H.; Gossard, A. C. Properties of Molecular Beam Epitaxially Grown ScAs: InGaAs and ErAs: InGaAs Nanocomposites for Thermoelectric Applications. *J. Cryst. Growth* **2011**, *316*, 56−59.

(7) Kawasaki, J. K.; Timm, R.; Delaney, K. T.; Lundgren, E.; Mikkelsen, A.; Palmstrøm, C. J. Local Density of States and Interface Effects in Semimetallic ErAs Nanoparticles Embedded in GaAs. *Phys. Rev. Lett.* **2011**, *107*, 036806.

(8) Kawasaki, J.; Schultz, B.; Palmstrøm, C. Size Effects on the Electronic Structure of ErSb Nanoparticles Embedded in the GaSb (001) Surface. *Phys. Rev. B* **2013**, *87*, 035419.

(9) Lu, H.; Ouellette, D. G.; Preu, S.; Watts, J. D.; Zaks, B.; Burke, P. G.; Sherwin, M. S.; Gossard, A. C. Self-Assembled ErSb Nanostructures with Optical Applications in Infrared and Terahertz. *Nano Lett.* **2014**, *14*, 1107−1112.

(10) Krivoy, E. M.; Vasudev, A. P.; Rahimi, S.; Synowicki, R. A.; McNicholas, K. M.; Ironside, D. J.; Salas, R.; Kelp, G.; Jung, D.; Nair, H. P.; Shvets, G.; Akinwande, D.; Lee, M. L.; Brongersma, M. L.;

Bank, S. R. Rare-Earth Monopnictide Alloys for Tunable, Epitaxial, Designer Plasmonics. *ACS Photonics* **2018**, *5*, 3051−3056.
(11) He, J.; Zhang, C.; Ghimire, N. J.; Liang, T.; Jia, C.; Jiang, J.; Tang, S.; Chen, S.; He, Y.; Mo, S.-K.; Hwang, C. C.; Hashimoto, M.; Lu, D. H.; Moritz, B.; et al. Distinct Electronic Structure for the Extreme Magnetoresistance in YSb. *Phys. Rev. Lett.* **2016**, *117*, 267201.
(12) Tafti, F.; Gibson, Q.; Kushwaha, S.; Haldolaarachchige, N.; Cava, R. Resistivity Plateau and Extreme Magnetoresistance in LaSb. *Nat. Phys.* **2016**, *12*, 272−277.
(13) Zeng, L.-K.; Lou, R.; Wu, D.-S.; Xu, Q. N.; Guo, P.-J.; Kong, L.-Y.; Zhong, Y.-G.; Ma, J.-Z.; Fu, B.-B.; Richard, P.; Wang, P.; Liu, G. T.; Lu, L.; Huang, Y.-B.; et al. Compensated Semimetal LaSb with Unsaturated Magnetoresistance. *Phys. Rev. Lett.* **2016**, *117*, 127204.
(14) Wu, Y.; Kong, T.; Wang, L.-L.; Johnson, D. D.; Mou, D.; Huang, L.; Schrunk, B.; Bud'ko, S. L.; Canfield, P. C.; Kaminski, A. Asymmetric Mass Acquisition in LaBi: Topological Semimetal Candidate. *Phys. Rev. B* **2016**, *94*, 081108.
(15) Nayak, J.; Wu, S.-C.; Kumar, N.; Shekhar, C.; Singh, S.; Fink, J.; Rienks, E. E.; Fecher, G. H.; Parkin, S. S.; Yan, B.; Felser, C. Multiple Dirac Cones at the Surface of the Topological Metal LaBi. *Nat. Commun.* **2017**, *8*, 1−5.
(16) Lou, R.; Fu, B.-B.; Xu, Q. N.; Guo, P.-J.; Kong, L.-Y.; Zeng, L.-K.; Ma, J.-Z.; Richard, P.; Fang, C.; Huang, Y.-B.; Sun, S.-S.; Wang, Q.; Wang, L.; Shi, Y.-G.; et al. Evidence of Topological Insulator State in the Semimetal LaBi. *Phys. Rev. B* **2017**, *95*, 115140.
(17) Kuroda, K.; Ochi, M.; Suzuki, H. S.; Hirayama, M.; Nakayama, M.; Noguchi, R.; Bareille, C.; Akebi, S.; Kunisada, S.; Muro, T.; Watson, M. D.; Kitazawa, H.; Haga, Y.; Kim, T. K.; et al. Experimental Determination of the Topological Phase Diagram in Cerium Monopnictides. *Phys. Rev. Lett.* **2018**, *120*, 086402.
(18) Schrunk, B.; Kushnirenko, Y.; Kuthanazhi, B.; Ahn, J.; Wang, L.-L.; O'Leary, E.; Lee, K.; Eaton, A.; Fedorov, A.; Lou, R.; Voroshnin, V.; Clark, O. J.; Sanchez-Barriga, J.; Bud'ko, S. L.; et al. Emergence of Fermi Arcs Due to Magnetic Splitting in an Antiferromagnet. *Nature* **2022**, *603*, 610−615.
(19) Allen, S., Jr.; Tabatabaie, N.; Palmstrøm, C.; Mounier, S.; Hull, G.; Sands, T.; DeRosa, F.; Gilchrist, H.; Garrison, K. Magneto-Transport in Ultrathin ErAs Epitaxial Layers Buried in GaAs. *Surf. Sci.* **1990**, *228*, 13−15.
(20) Bernevig, B. A.; Hughes, T. L.; Zhang, S.-C. Quantum Spin Hall Effect and Topological Phase Transition in HgTe Quantum Wells. *Science* **2006**, *314*, 1757−1761.
(21) Konig, M.; Wiedmann, S.; Brune, C.; Roth, A.; Buhmann, H.; Molenkamp, L. W.; Qi, X.-L.; Zhang, S.-C. Quantum Spin Hall Insulator State in HgTe Quantum Wells. *Science* **2007**, *318*, 766−770.
(22) Qian, X.; Liu, J.; Fu, L.; Li, J. Quantum Spin Hall Effect in Two-Dimensional Transition Metal Dichalcogenides. *Science* **2014**, *346*, 1344−1347.
(23) Tang, S.; Zhang, C.; Wong, D.; Pedramrazi, Z.; Tsai, H.-Z.; Jia, C.; Moritz, B.; Claassen, M.; Ryu, H.; Kahn, S.; Jiang, J.; Yan, H.; Hashimoto, M.; Lu, D.; et al. Quantum Spin Hall State in Monolayer 1T'-WTe_2. *Nat. Phys.* **2017**, *13*, 683−687.
(24) Fei, Z.; Palomaki, T.; Wu, S.; Zhao, W.; Cai, X.; Sun, B.; Nguyen, P.; Finney, J.; Xu, X.; Cobden, D. H. Edge Conduction in Monolayer WTe_2. *Nat. Phys.* **2017**, *13*, 677−682.
(25) Wu, S.; Fatemi, V.; Gibson, Q. D.; Watanabe, K.; Taniguchi, T.; Cava, R. J.; Jarillo-Herrero, P. Observation of the Quantum Spin Hall Effect up to 100 K in a Monolayer Crystal. *Science* **2018**, *359*, 76−79.
(26) Haruyama, J. Quantum-Spin-Hall Phases and 2D Topological Insulating States in Atomically Thin Layers. *J. Appl. Phys.* **2021**, *129*, 090902.
(27) Tang, P.; Chen, P.; Cao, W.; Huang, H.; Cahangirov, S.; Xian, L.; Xu, Y.; Zhang, S.-C.; Duan, W.; Rubio, A. Stable Two-Dimensional Dumbbell Stanene: A Quantum Spin Hall Insulator. *Phys. Rev. B* **2014**, *90*, 121408.
(28) Liu, J.; Wang, H.; Fang, C.; Fu, L.; Qian, X. Van der Waals Stacking-Induced Topological Phase Transition in Layered Ternary Transition Metal Chalcogenides. *Nano Lett.* **2017**, *17*, 467−475.
(29) Kandrai, K.; Vancsó, P.; Kukucska, G.; Koltai, J.; Baranka, G.; Hoffmann, Á.; Pekker, Á.; Kamarás, K.; Horváth, Z. E.; Vymazalová; Tapaszto, L.; Nemes-Incze, P. Signature of Large-Gap Quantum Spin Hall State in the Layered Mineral Jacutingaite. *Nano Lett.* **2020**, *20*, 5207−5213.
(30) Khalid, S.; Sharan, A.; Janotti, A. Hybrid Functional Calculations of Electronic Structure and Carrier Densities in Rare-Earth Monopnictides. *Phys. Rev. B* **2020**, *101*, 125105.
(31) Kane, C. L.; Mele, E. J. Quantum Spin Hall Effect in Graphene. *Phys. Rev. Lett.* **2005**, *95*, 226801.
(32) Sheng, L.; Sheng, D.; Ting, C.; Haldane, F. Nondissipative Spin Hall Effect via Quantized Edge Transport. *Phys. Rev. Lett.* **2005**, *95*, 136602.
(33) Fu, L.; Kane, C. L. Topological Insulators with Inversion Symmetry. *Phys. Rev. B* **2007**, *76*, 045302.
(34) Fukui, T.; Hatsugai, Y. Quantum Spin Hall Effect in Three-Dimensional Materials: Lattice Computation of Z2 Topological Invariants and Its Application to Bi and Sb. *J. Phys. Soc. Jpn.* **2007**, *76*, 053702.
(35) Sancho, M. L.; Sancho, J. L.; Sancho, J. L.; Rubio, J. Highly Convergent Schemes for the Calculation of Bulk and Surface Green Functions. *J. Phys. F: Met. Phys.* **1985**, *15*, 851.
(36) Qi, X.-L.; Zhang, S.-C. The Quantum Spin Hall Effect and Topological Insulators. *Phys. Today* **2010**, *63*, 33−38.
(37) Maciejko, J.; Hughes, T. L.; Zhang, S.-C. The Quantum Spin Hall Effect. *Annu. Rev. Condens. Matter Phys.* **2011**, *2*, 31−53.
(38) Khalid, S.; Janotti, A. Trivial to Nontrivial Topology Transition in Rare-Earth Pnictides with Epitaxial Strain. *Phys. Rev. B* **2020**, *102*, 035151.
(39) Inbar, H. S.; Ho, D. Q.; Chatterjee, S.; Engel, A. N.; Khalid, S.; Dempsey, C. P.; Pendharkar, M.; Chang, Y. H.; Nishihaya, S.; Fedorov, A. V.; Lu, D.; Hashimoto, M.; Read, D.; Janotti, A.; Palmstrøm, C. J. Strain Tuning the Band Topology of Epitaxial GdSb Quantum Wells. *arXiv*, November 28, 2022. DOI: 10.48550/arXiv.2211.15806 (accessed on July 16, 2023).
(40) Chang, Y. J.; Kim, C. H.; Phark, S.-H.; Kim, Y.; Yu, J.; Noh, T. Fundamental Thickness Limit of Itinerant Ferromagnetic $SrRuO_3$ Thin Films. *Phys. Rev. Lett.* **2009**, *103*, 057201.
(41) Sohn, B.; Kim, J. R.; Kim, C. H.; Lee, S.; Hahn, S.; Kim, Y.; Huh, S.; Kim, D.; Kim, Y.; Kyung, W.; Kim, M.; Kim, M.; Noh, T. W.; Kim, C. Observation of Metallic Electronic Structure in a Single-Atomic-Layer Oxide. *Nat. Commun.* **2021**, *12*, 1−8.
(42) Hulliger, F. Non-Metallic Compounds—II. In *Handbook on the Physics and Chemistry of Rare Earths*; Elsevier, 1979; Vol. *4*, pp 153−236.
(43) Duan, C.-G.; Sabiryanov, R. F.; Mei, W.-N.; Dowben, P. A.; Jaswal, S.; Tsymbal, E. Y. Magnetic Ordering in Gd Monopnictides: Indirect Exchange Versus Superexchange Interaction. *Appl. Phys. Lett.* **2006**, *88*, 182505.
(44) Duan, C.-G.; Sabirianov, R.; Mei, W.-N.; Dowben, P. A.; Jaswal, S.; Tsymbal, E. Y. Electronic, Magnetic and Transport Properties of Rare-Earth Monopnictides. *J. Phys.: Condens. Matter* **2007**, *19*, 315220.
(45) Kushnirenko, Y.; Schrunk, B.; Kuthanazhi, B.; Wang, L.-L.; Ahn, J.; O'Leary, E.; Eaton, A.; Bud'ko, S. L.; Slager, R.-J.; Canfield, P. C.; Kaminski, A. Rare-Earth Monopnictides: Family of Antiferromagnets Hosting Magnetic Fermi Arcs. *Phys. Rev. B* **2022**, *106*, 115112.
(46) Niu, C.; Wang, H.; Mao, N.; Huang, B.; Mokrousov, Y.; Dai, Y. Antiferromagnetic Topological Insulator with Nonsymmorphic Protection in Two Dimensions. *Phys. Rev. Lett.* **2020**, *124*, 066401.
(47) Liang, A.; Chen, C.; Zheng, H.; Xia, W.; Huang, K.; Wei, L.; Yang, H.; Chen, Y.; Zhang, X.; Xu, X.; Wang, M.; Guo, Y.; Yang, L.; Liu, Z.; Chen, Y. Approaching a Minimal Topological Electronic Structure in Antiferromagnetic Topological Insulator $MnBi_2Te_4$ via Surface Modification. *Nano Lett.* **2022**, *22*, 4307−4314.
(48) Xu, R.; Bai, Y.; Zhou, J.; Li, J.; Gu, X.; Qin, N.; Yin, Z.; Du, X.; Zhang, Q.; Zhao, W.; Li, Y.; Wu, Y.; Ding, C.; Wang, L.; et al.

Evolution of the Electronic Structure of Ultrathin $MnBi_2Te_4$ Films. *Nano Lett.* **2022**, *22*, 6320−6327.
(49) Li, Z.; Kim, J.; Kioussis, N.; Ning, S.-Y.; Su, H.; Iitaka, T.; Tohyama, T.; Yang, X.; Zhang, J.-X. GdN Thin Film: Chern Insulating State on Square Lattice. *Phys. Rev. B* **2015**, *92*, 201303.
(50) Inoue, H.; Han, M.; Hu, M.; Suzuki, T.; Liu, J.; Checkelsky, J. G. Band Engineering of a Magnetic Thin Film Rare-Earth Monopnictide: a Platform for High Chern Number. *Phys. Rev. Mater.* **2019**, *3*, 101202.
(51) Inbar, H. S.; Ho, D. Q.; Chatterjee, S.; Pendharkar, M.; Engel, A. N.; Dong, J. T.; Khalid, S.; Chang, Y. H.; Guo, T.; Fedorov, A. V.; Lu, D.; Hashimoto, M.; Read, D.; Janotti, A.; Palmstrøm, C. J. Epitaxial Growth, Magnetoresistance, and Electronic Band Structure of GdSb Magnetic Semimetal Films. *Phys. Rev. Mater.* **2022**, *6*, L121201.
(52) Chatterjee, S.; Khalid, S.; Inbar, H. S.; Goswami, A.; Guo, T.; Chang, Y.-H.; Young, E.; Fedorov, A. V.; Read, D.; Janotti, A.; Palmstrøm, C. J. Controlling Magnetoresistance by Tuning Semimetallicity through Dimensional Confinement and Heteroepitaxy. *Sci. Adv.* **2021**, *7*, eabe8971.
(53) Hohenberg, P.; Kohn, W. Inhomogeneous Electron Gas. *Phys. Rev.* **1964**, *136*, B864−B871.
(54) Kohn, W.; Sham, L. J. Self-Consistent Equations Including Exchange and Correlation Effects. *Phys. Rev.* **1965**, *140*, A1133−A1138.
(55) Kresse, G.; Furthmüller, J. Efficient Iterative Schemes for Ab Initio Total-Energy Calculations Using a Plane-Wave Basis Set. *Phys. Rev. B* **1996**, *54*, 11169−11186.
(56) Kresse, G.; Furthmüller, J. Efficiency of Ab-Initio Total Energy Calculations for Metals and Semiconductors Using a Plane-Wave Basis Set. *Comput. Mater. Sci.* **1996**, *6*, 15−50.
(57) Blöchl, P. E. Projector Augmented-Wave Method. *Phys. Rev. B* **1994**, *50*, 17953−17979.
(58) Kresse, G.; Joubert, D. From Ultrasoft Pseudopotentials to the Projector Augmented-Wave Method. *Phys. Rev. B* **1999**, *59*, 1758.
(59) Heyd, J.; Scuseria, G. E.; Ernzerhof, M. Hybrid Functionals Based on a Screened Coulomb Potential. *J. Chem. Phys.* **2003**, *118*, 8207−8215.
(60) Krukau, A. V.; Vydrov, O. A.; Izmaylov, A. F.; Scuseria, G. E. Influence of the Exchange Screening Parameter on the Performance of Screened Hybrid Functionals. *J. Chem. Phys.* **2006**, *125*, 224106.
(61) Perdew, J. P.; Burke, K.; Ernzerhof, M. Generalized Gradient Approximation Made Simple. *Phys. Rev. Lett.* **1996**, *77*, 3865.
(62) Perdew, J. P.; Burke, K.; Ernzerhof, M. Generalized Gradient Approximation Made Simple [Phys. Rev. Lett. 77, 3865 (1996)]. *Phys. Rev. Lett.* **1997**, *78*, 1396.
(63) Ozaki, T. Variationally Optimized Atomic Orbitals for Large-Scale Electronic Structures. *Phys. Rev. B* **2003**, *67*, 155108.
(64) Ozaki, T.; Kino, H. Numerical Atomic Basis Orbitals from H to Kr. *Phys. Rev. B* **2004**, *69*, 195113.
(65) Ozaki, T.; Kino, H. Efficient Projector Expansion for the Ab Initio LCAO Method. *Phys. Rev. B* **2005**, *72*, 045121.
(66) Morrison, I.; Bylander, D.; Kleinman, L. Nonlocal Hermitian Norm-conserving Vanderbilt Pseudopotential. *Phys. Rev. B* **1993**, *47*, 6728.
(67) Pizzi, G.; Vitale, V.; Arita, R.; Blügel, S.; Freimuth, F.; Géranton, G.; Gibertini, M.; Gresch, D.; Johnson, C.; Koretsune, T.; Ibanez-Azpiroz, J.; Lee, H.; Lihm, J.-M.; Marchand, D.; et al. Wannier90 as a Community Code: New Features and Applications. *J. Phys.: Condens. Matter* **2020**, *32*, 165902.
(68) Wu, Q.; Zhang, S.; Song, H.-F.; Troyer, M.; Soluyanov, A. A. WannierTools: An Open-Source Software Package for Novel Topological Materials. *Comput. Phys. Commun.* **2018**, *224*, 405−416.
(69) Soluyanov, A. A.; Vanderbilt, D. Wannier Representation of Z2 Topological Insulators. *Phys. Rev. B* **2011**, *83*, 035108.
(70) Xiao, J.; Yan, B. First-Principles Calculations for Topological Quantum Materials. *Nat. Rev. Phys.* **2021**, *3*, 283−297.
(71) Yu, R.; Qi, X. L.; Bernevig, A.; Fang, Z.; Dai, X. Equivalent Expression of Z2 Topological Invariant for Band Insulators Using the Non-Abelian Berry Connection. *Phys. Rev. B* **2011**, *84*, 075119.
(72) Gao, J.; Wu, Q.; Persson, C.; Wang, Z. Irvsp: to Obtain Irreducible Representations of Electronic States in the VASP. *Comput. Phys. Commun.* **2021**, *261*, 107760.
(73) Chua, K.; Pratt, J. A Simple Direct-Reaction Calorimeter and Some Observations on the Heats of Formation of IIIA-VB Sodium Chloride Structures. *Thermochim. Acta* **1974**, *8*, 409−421.

https://doi.org/10.1021/acsnano.3c03307
ACS Nano 2023, 17, 20991−20998